

Article

LiDAR Validation of a Video-Derived Beachface Topography on a Tidal Flat

David Didier ^{1,*}, Pascal Bernatchez ¹, Emmanuel Augereau ², Charles Caulet ²,
Dany Dumont ³ , Eliott Bismuth ¹, Louis Cormier ¹, France Floc'h ² and Christophe Delacourt ²

¹ Québec-Océan, Centre d'études nordiques, Chaire de Recherche en Géoscience Côtière, Université du Québec à Rimouski, Rimouski, QC G5L 3A1, Canada; Pascal_Bernatchez@uqar.ca (P.B.); Eliott_Bismuth@uqar.ca (E.B.); Louis_Cormier@uqar.ca (L.C.)

² Laboratoire Géosciences Océan UMR 6538, Institut Universitaire Européen de la mer, Université de Bretagne Occidentale, Brest, 29280 Plouzané, France; emmanuel.augereau@univ-brest.fr (E.A.); charles.caulet@univ-brest.fr (C.C.); france.floch@univ-brest.fr (F.F.); christophe.delacourt@univ-brest.fr (C.D.)

³ Institut des Sciences de la mer de Rimouski, Université du Québec à Rimouski, Québec-Océan, Physique des Océans—Laboratoire de Rimouski, Rimouski, QC, G5L 3A1, Canada; Dany_Dumont@uqar.ca

* Correspondence: David_Didier@uqar.ca; Tel.: +1-418-723-1986 (ext. 1364)

Received: 26 June 2017; Accepted: 7 August 2017; Published: 11 August 2017

Abstract: Increasingly used shore-based video stations enable a high spatiotemporal frequency analysis of shoreline migration. Shoreline detection techniques combined with hydrodynamic conditions enable the creation of digital elevation models (DEMs). However, shoreline elevations are often estimated based on nearshore process empirical equations leading to uncertainties in video-based topography. To achieve high DEM correspondence between both techniques, we assessed video-derived DEMs against LiDAR surveys during low energy conditions. A newly installed video system on a tidal flat in the St. Lawrence Estuary, Atlantic Canada, served as a test case. Shorelines were automatically detected from time-averaged (TIMEX) images using color ratios in low energy conditions synchronously with mobile terrestrial LiDAR during two different surveys. Hydrodynamic (waves and tides) data were recorded in-situ, and established two different cases of water elevation models as a basis for shoreline elevations. DEMs were created and tested against LiDAR. Statistical analysis of shoreline elevations and migrations were made, and morphological variability was assessed between both surveys. Results indicate that the best shoreline elevation model includes both the significant wave height and the mean water level. Low energy conditions and in-situ hydrodynamic measurements made it possible to produce video-derived DEMs virtually as accurate as a LiDAR product, and therefore make an effective tool for coastal managers.

Keywords: video monitoring; shoreline detection; beach morphology; mobile terrestrial LiDAR; erosion; Atlantic Canada

1. Introduction

Beaches evolve through time and space, influenced by morphogenetic processes occurring in multiple dimensions in the surf and swash zones [1]. Following wave breaking, different short-term dynamic processes occur on a beach, mostly wave-induced high/low-frequency swash motions [2], groundwater/bed interactions [3,4], and scouring [5]. The beach morphology usually tends toward an equilibrium slope resulting from an onshore/offshore sediment transport induced by waves and currents [6–8]. Changes also occur on longer time scales where beaches are affected by strong seasonal cycles. For example, in cold regions, the presence of sea ice can protect (i.e., consolidates beach sediments) or erode (i.e., scouring at the icefoot's toe, transport by drift ice, etc.) the beach profile [9].

Multi-year analyses of the shoreline position can show variabilities on a kilometer scale on sandy coasts [10,11], while geologically constrained and protected systems like platform-beaches [12,13] and pocket-beaches [14] can show little changes. Capturing relevant morphogenic processes across different scales is not straightforward, namely because of the low temporal resolution of most monitoring strategies (large time interval between field campaigns) [10] that filter short-term events. Along with climate change and sea-level rise, beach morphodynamics can therefore be confusing and misunderstood by coastal managers and engineers in need of operational tools in order to deal with constantly evolving beaches [15]. On erosion hotspots [16], it is imperative to better understand the multi-scale variability of the beach morphology and slope, which are essential for flood risk assessment and to design protective structures in suitable adaptation strategies.

Out of many technological tools for beach morphology monitoring such as total stations [17], DGPS surveys [18–20], radar [21], UAV [22–24], or LiDAR [25–27], perhaps the shore-based video imagery is the most versatile. Such systems can be installed virtually everywhere for continuous recording over a long period of time [28], and are not directly vulnerable to extreme events as opposed to in-situ instruments [29]. In terms of spatiotemporal resolutions, video cameras offer other great perspectives, enabling both short-term and long-term monitoring capabilities. Video imagery is clearly effective for wave runup measurements, including swash and setup [30–33]. It then can be applied to calibrate empirical formulae in low and high energy situations through time-stack analysis [34,35]. Applied on video imagery, shoreline detection techniques based on time-exposure images can also acquire high-frequency topographical information when combined with hydrodynamic forcing [36–38]. With a relatively low cost [39], one can obtain digital elevation models (DEMs) with a few centimetres accuracy [37]. However, such systems and subsequent image analysis needs to be adapted to local conditions, since relationships between image optical characteristics and environmental/geometrical conditions on beaches are not always understood [40], especially in cold environments where coastal sea ice interferes with sediment dynamics [41].

A video-based shoreline evolution monitoring typically integrates two parameters: the shoreline detection and the water elevation model [42]. Swash and wave breaking on reflective beaches typically enhance beach/water pixel gradient intensities, seen as foamy bright bands, facilitating its detection using grey-scale images [43,44]. However, detecting shorelines on dissipative beaches with large surf zones is not as straightforward since the cross-shore pixel intensities/variance due to waves and foam motions [38] is scattered along a larger area. Another problem arises in enclosed areas with less energetic conditions such as estuaries [45], or on the landward side of sandbars [37]. To avoid these problems, some authors have proposed shoreline detection techniques based on full color characteristics of the imagery, especially using ARGUS stations [42,46], as opposed to traditional grey-scale image analysis developed earlier [43]. Almar et al. [37] also detected shorelines based on color analysis, but added a correction due to alongshore swash shapes at different tidal levels to estimate the intertidal topography at a double-barred and energetic meso-tidal beach in Biscarrose, France. The resulting morphology performed well with GPS validation runs for low energetic conditions (significant wave height, $H_s < 1$ m). Detected planimetric shorelines can be compared to GPS runs on the beach at the time of the detection, with horizontal uncertainties generally varying between ~1 and 6 m [42,45,47].

The water elevation associated with a detected shoreline commonly includes the still water level (astronomical tide plus the barometric surge), and wave-induced runup (including setup and swash) [10,37,47,48]. The former component, the offshore static water level, is mostly known with in-situ gauge prior wave breaking. The latter is more complicated to obtain, since foreshore dynamics are most notably deduced with empirical formulations. Aarninkhof et al. [42] computed the setup and swash oscillation elevations, and concluded that their technique detected a shoreline at the upper end of the swash runup. Apart from uncertainties in planimetric shoreline detections and inherent to RTK-GPS validations and ground control points, these techniques imply uncertainties associated with the empirical formulations used. Such equations are limited to the input conditions only, and

common vertical errors and deviations between theoretical results and observed values can range from 0.5 to 2 m [13,49,50]. In estuaries with mudflats, Morris et al. [45] used RTK-DGPS to validate video-derived shoreline elevations and obtained vertical errors within 5 cm. On more open coasts with moderate to high energy conditions, Vousdoukas et al. [47], Uunk et al. [36], and Aarninkhof et al. [42] also found low elevation error values using field DGPS validations, respectively of 26 cm, 28 cm, and 15 cm. Subsequent associations of detected shorelines with empirical formulations seems to show good results in most cases, but local validations appear to be necessary both for detected shorelines and the associated water levels. In low-energy environments such as estuaries and sandflats, the absence of significantly contrasting swash on the beach motivated this study.

Beaches along the St. Lawrence maritime Estuary (Atlantic Canada) typically show such characteristics. Furthermore, in such cold environments, the progressive disappearance of coastal sea ice during winter due to climate change leads to an enhancement of coastal erosion [51]. In order to analyze these multi-scale dynamics, efficient methodology to retrieve shoreline evolution is needed. This paper aims to create digital elevations models based on image-detected shorelines and to validate the video-derived topography on a low-energy meso-tidal beachface with a two-kilometer-wide sandflat. The shoreline elevations are obtained with in-situ wave and tidal gauges landward of the surf zone. Resulting digital elevation models are compared to simultaneous mobile LiDAR acquisition results. The LiDAR-interpolated topography acts as a validation tool for the video-based topography. Finally, the shoreline displacement rates during the autumn of 2016 are calculated from both video and LiDAR-based topography in order to compare both methods.

2. Materials and Methods

2.1. Study Area

The Manicouagan Peninsula is located on the north shore of the St. Lawrence maritime Estuary (Figure 1). This imposing delta was formed in the Goldthwait Sea during the last deglaciation. During the Laurentian transgression which ended around 4.4–4.2 ka years BP, an important erosion platform was carved in the fine prodeltaic sediments, forming today steep beachfaces over a sandy flat as wide as 2 km in the cross-shore direction [52].

Despite previous Quaternary [52–54], coastal erosion [51], and sea ice [55,56] studies in the area, little is known on the morphodynamics of the Manicouagan beaches. Coastal citizens are facing constant erosion and one of the hotspots is located on the beach of Pointe-Lebel (Figure 1c). Shrinking winter sea ice and its predicted disappearance in the second half of the 21st century [55,56] will potentially increase erosion problems during the cold season by enabling storm waves to reach the beach. Deposited beach materials in Pointe-Lebel consist mainly of coarse and medium sands coming from sedimentary coastal cliffs. Beach erosion reached around -1.2 m and -2.9 m/year (1931–2001) [51].

Tides around the Manicouagan Peninsula are semi-diurnal and meso-tidal, ranging between 3 and 4.3 m, and reaching up to 4.9 m during extreme spring tides [57], with currents reaching 3 m/s [58]. All tidal levels will be subsequently referred to their local geodetical datum (CGVD28), according to a difference of -1.81 m with the chart datum (mean sea levels (MSL) = 0 m; chart datum (CD) = -1.81 m; Higher high water large tide (HHWLT) = 2.89 m; Lower low water large tide (LLWLT) = -1.19 m). The Pointe-Lebel beach studied in this paper is characterized by a low-tide terrace/non-barred dissipative shape (considering the Masselink and Short [59] and Scott et al. [60] classifications). It is bounded by two small creeks forming deltas on the lower foreshore (see Figure 1c). The main longshore drift is oriented toward northeast [52]. The wide intertidal sandflat is covered in some places with sandy accumulation banks of low amplitude. At high tide, swash occurs on a more reflective beachface with an average width of 20 m. The beachface is delimited on its upper part by an erosion scarp and on its lower limit by a hinge line. This break of slope marks the beginning of the lower foreshore which stretches over more than 2 km at low tide.

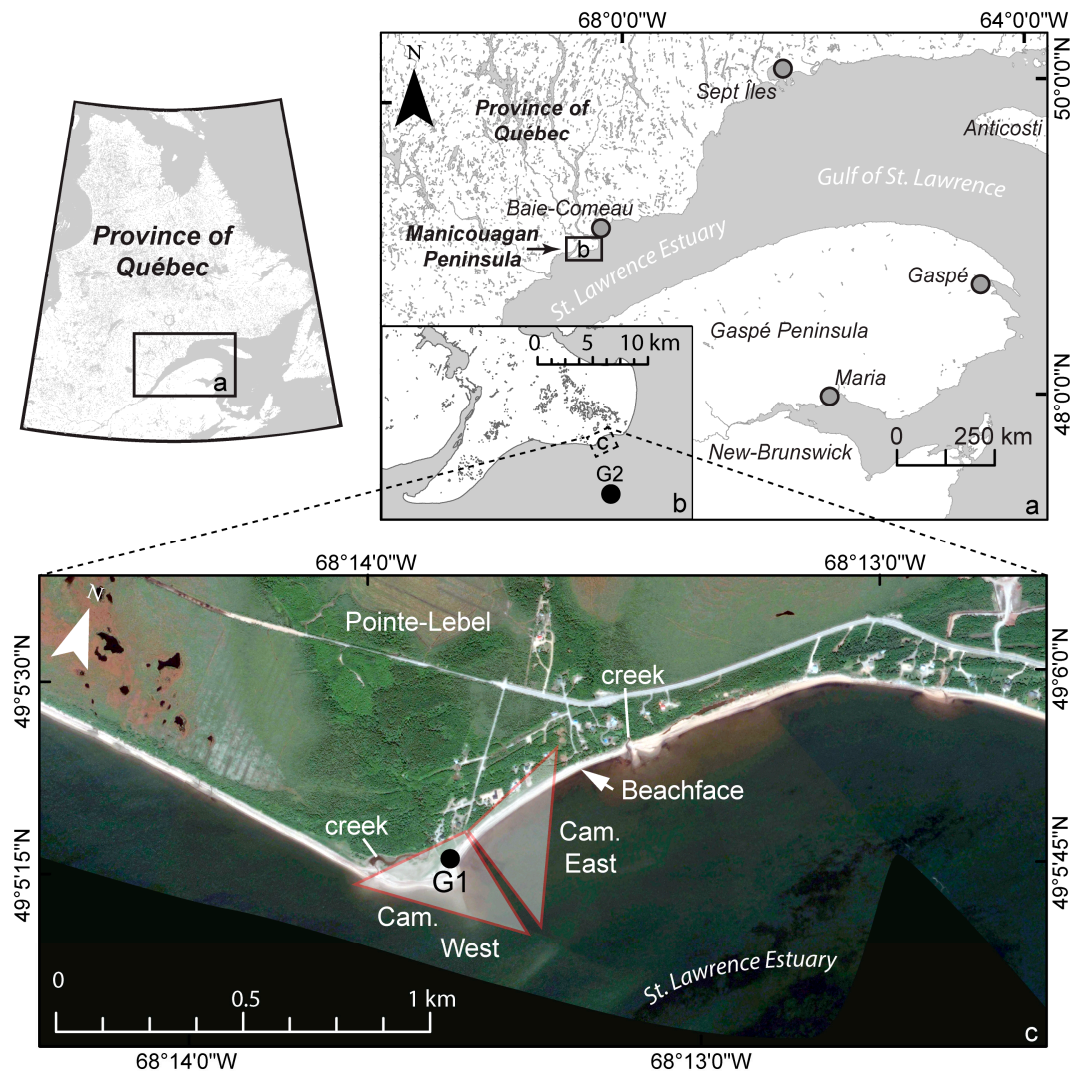


Figure 1. Location of the Manicouagan Peninsula (a,b) and of the monitoring station at Pointe-Label (c). Two video cameras are installed with 2 instruments (G1: nearshore pressure sensor logger; G2: offshore acoustic, wave and current meter (AWAC) for in-situ hydrodynamic acquisition (black circles) (b,c)).

The offshore wave climate is mainly generated from dominant westerlies and strong easterly winds [61]. Beaches of the Manicouagan Peninsula can be exposed to strong ENE winds blowing on a 350 km long fetch [53]. Being oriented ESE, this is especially the case of the Pointe-Label beach where the video camera system is located. Ruest et al. [56] simulated wave heights with winds from the Modern-Era Retrospective Analysis for Research and Applications (MERRA) re-analysis in the Estuary. Simulated extreme waves (99th percentile H_s) are between 1 and 2 m, while the 50-year return H_s is higher (between 2.5 and 4 m) for the whole Estuary. As per the authors, wave heights in the Gulf of St. Lawrence are going to increase by 5–10% by 2100 with extensive ice-free periods during winter.

2.2. Wave and Tidal Data

Waves were measured with an array of two in-situ gauges between 1 July 2016 and 30 December 2016 (Figure 2). The first sensor (RBR Virtuoso) is located at the toe of the beachface close to the break in the foreshore slope (G1, $z = 0.20$ m), landward of the tidal flat. This nearshore sensor acquired continuous total pressures at a 4 Hz frequency, and was subsequently processed through a spectral

analysis over a length of 1024 s (17.06 min). Offshore waves were acquired at 2 Hz with an Acoustic Wave and Current meter (AWAC) deployed at 14 m depth (G2) (Figure 2b) southeast of Pointe-Lebel. The cross-shore distance of both instruments from the HHWLT line on the beach is respectively 23 m and 4.5 km offshore. Calculated spectral wave parameters are the significant wave height (H_s), mean periods (T_{m02}), and offshore mean wave directions θ at G2. Atmospheric pressure was obtained from a barometric pressure gauge (HOBO data logger) every 10 min and interpolated to wave sampling rates. Mean water level (η) was calculated from mean pressure on both instruments.

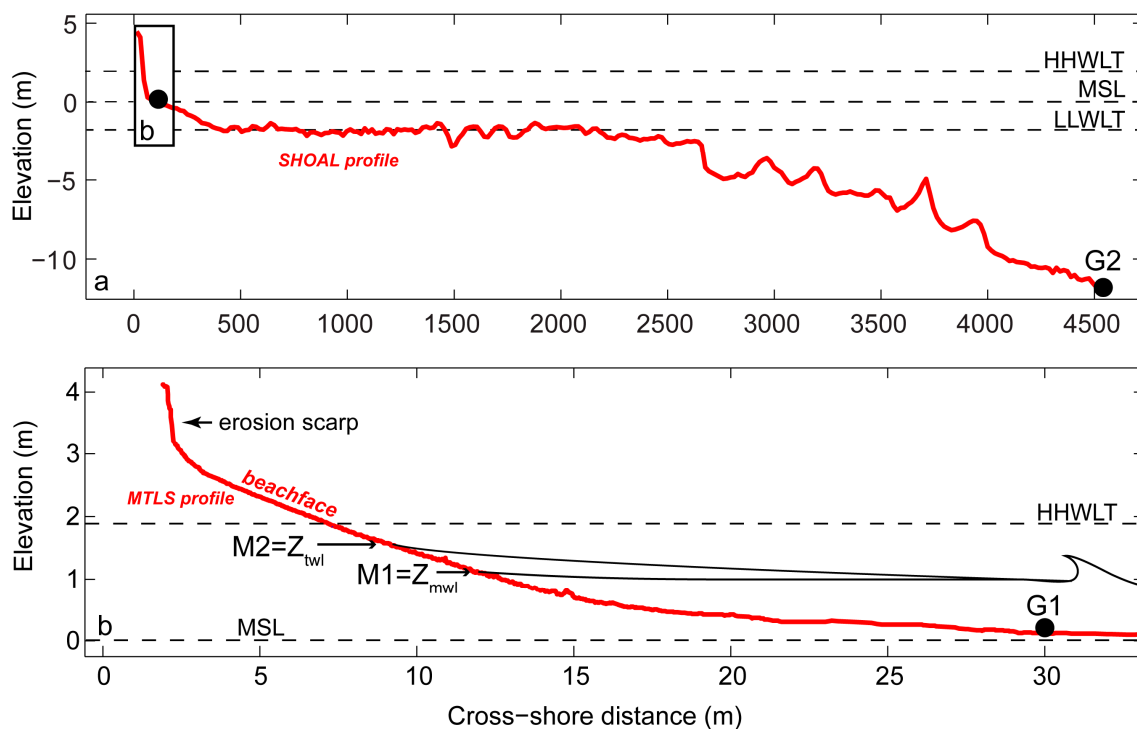


Figure 2. Cross-shore profile (extracted from a shoal survey of 2015 obtain from the Canadian Hydrographic Service, 2015) of Pointe-Lebel beach and location of the in-situ instruments (G1 and G2) (a). A focus on the beachface is shown in (b) from the MTLs (Mobile Terrestrial Lidar System) survey of 3 August 2016. Elevations associated to higher high water large tides (HHWLT), mean sea levels (MSL) and lower low water large tides (LLWLT) are shown by horizontal dashed lines.

Mean water level fluctuations recorded offshore during the entire joint deployment period oscillated between -2.42 and 3.17 m. The sensor G1 recorded a maximum H_s of 0.98 m on 16 November 2016. During the LiDAR surveys of 3 August and 18 November (vertical lines on Figure 3), the conditions were calm and the maximum mean water levels at G1 reached 1.48 m and 2.25 m at high tide, respectively. Significant wave heights did not exceed 0.14 m during the surveys.

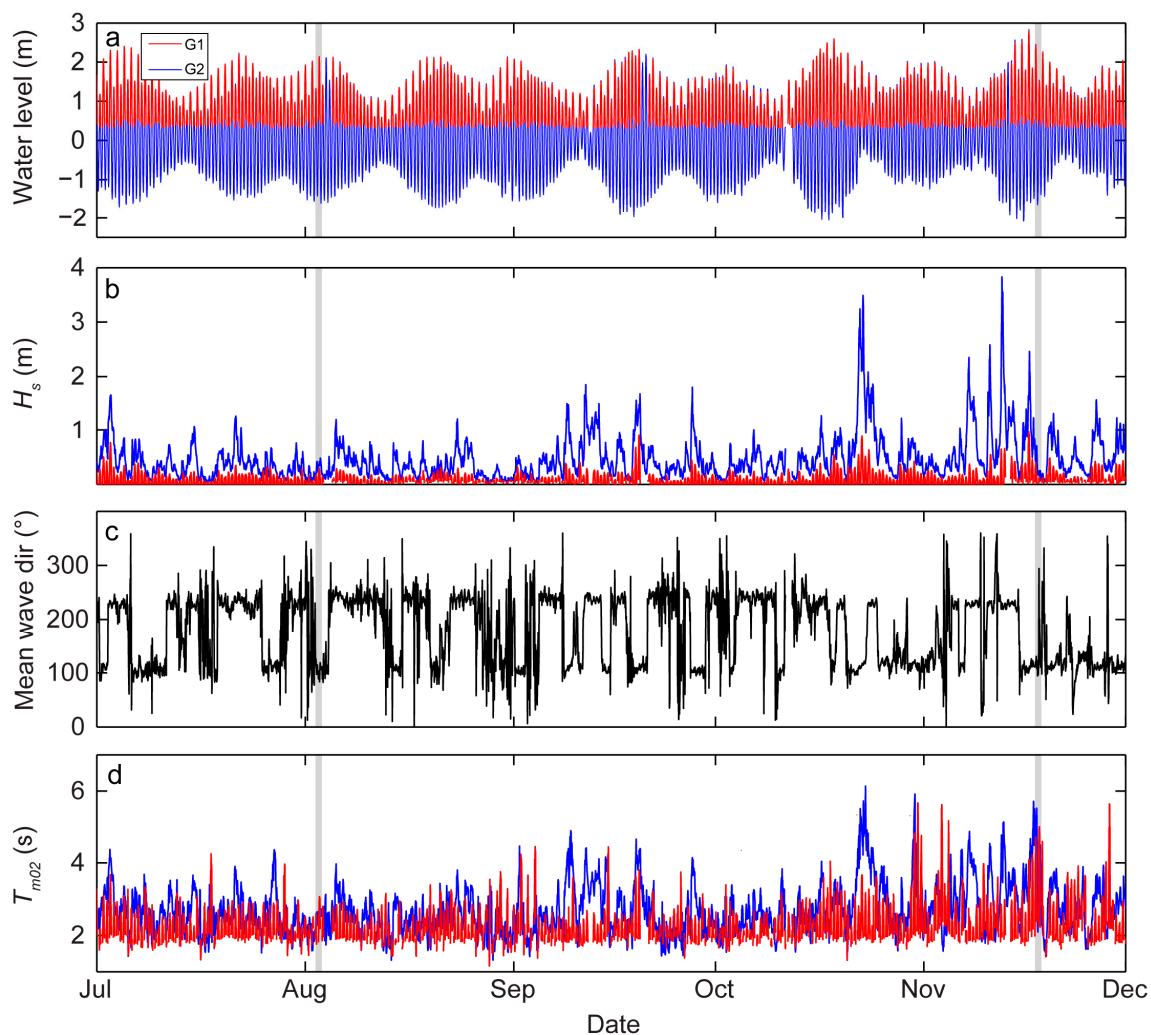


Figure 3. Mean water level (with daily tidal cycles) (m) (a), significant wave height (m) (b), mean wave direction ($^{\circ}$) (c), and period (s) (d) recorded between July and December 2016. The surveys of 3 August and 18 November 2016 are shown by vertical grey bands.

During the autumn of 2016 (September to December), more energetic events were observed. Offshore significant wave heights reached a maximum of 3.8 m at G2 on 12 November, but it happened at low tide and dissipation across the tidal flat prevented incoming waves to reach the beach. On 16 November, waves at the beachface toe reached 0.92 m, and mean wave directions (observed offshore) spanned between 99° and 123° (ESE) throughout the day.

2.3. LiDAR Survey and Topographic Data

A Mobile Terrestrial LiDAR System (MTLS), hereinafter referred to as LiDAR, was used to acquire a high-resolution beach topography on 3 August 2016 (Figure 4) and 18 November 2016. Both surveys were conducted at low tide. The LiDAR is mounted on a utility side by side vehicle (Figure 5b) moving at $\sim 30\text{--}40$ km/h. The system includes a laser scanner Riegl VQ-250 and a GPS inertial navigation system Applanix POS-LV 220. Post-processing for raw data analysis is described in Didier et al. [62]. A manual filtering of the debris on the beach was made on the raw LiDAR data (dense point cloud) to delete trees and driftwood from the final LiDAR topography. The RMS errors (x, y, z) (23 control points) between RTK-GPS (Trimble R8) and adjacent laser points was assessed in Didier et al. [62] and are in the order ± 0.03 m [62]. The LiDAR data were used as a validation surface for each detected and orthorectified shoreline.

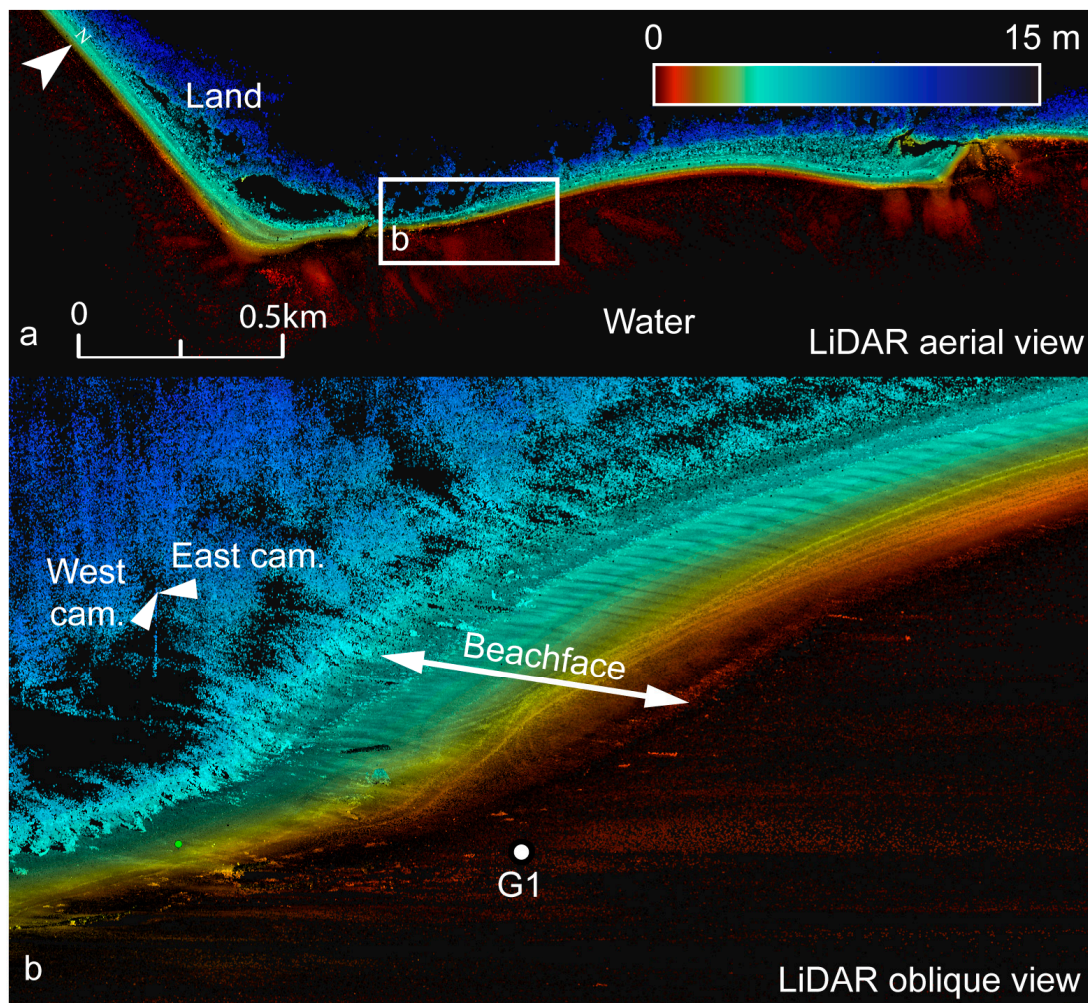


Figure 4. LiDAR point cloud from the survey of 3 August 2016 on the beach of Pointe-Lébel shown in aerial (a) and perspective (b) views.

2.4. Video Monitoring Station

The beach of Pointe-Lébel was equipped with two AXIS P3367-VE video camera systems on 8 June 2016 (Figures 4b and 5). Both cameras are installed on a pole originally located at 5 m from the beach (49.092°N , 68.227°W). The system is directly connected to a power grid. Each camera covers a pan range of 84° and a shadow zone varying from ~ 1 m near the system to ~ 10 m at the beachface toe is located between both camera views (no overlap between views). The total view reaches $\sim 180^{\circ}$. Cameras are precisely located at 12.08 m above the mean sea level and offer a continuous sampling acquisition of 4 Hz (2592×1944 pixels, 5 megapixels) during daylight (~ 10 h/day). Both Power Over the Ethernet (POE) IP cameras are accessible online for remote modifications via a 4G network, and are connected on a laptop computer (Lenovo Intel[®] Core[™] i5-6200 U CPU, 2.3 GHz–2.4 GHz, 8 Go RAM, 64 bits) located in a sealed box on the system post. All videos are recorded directly on physical hard drives to assure and secure data acquisition during all weather conditions, particularly during winter.

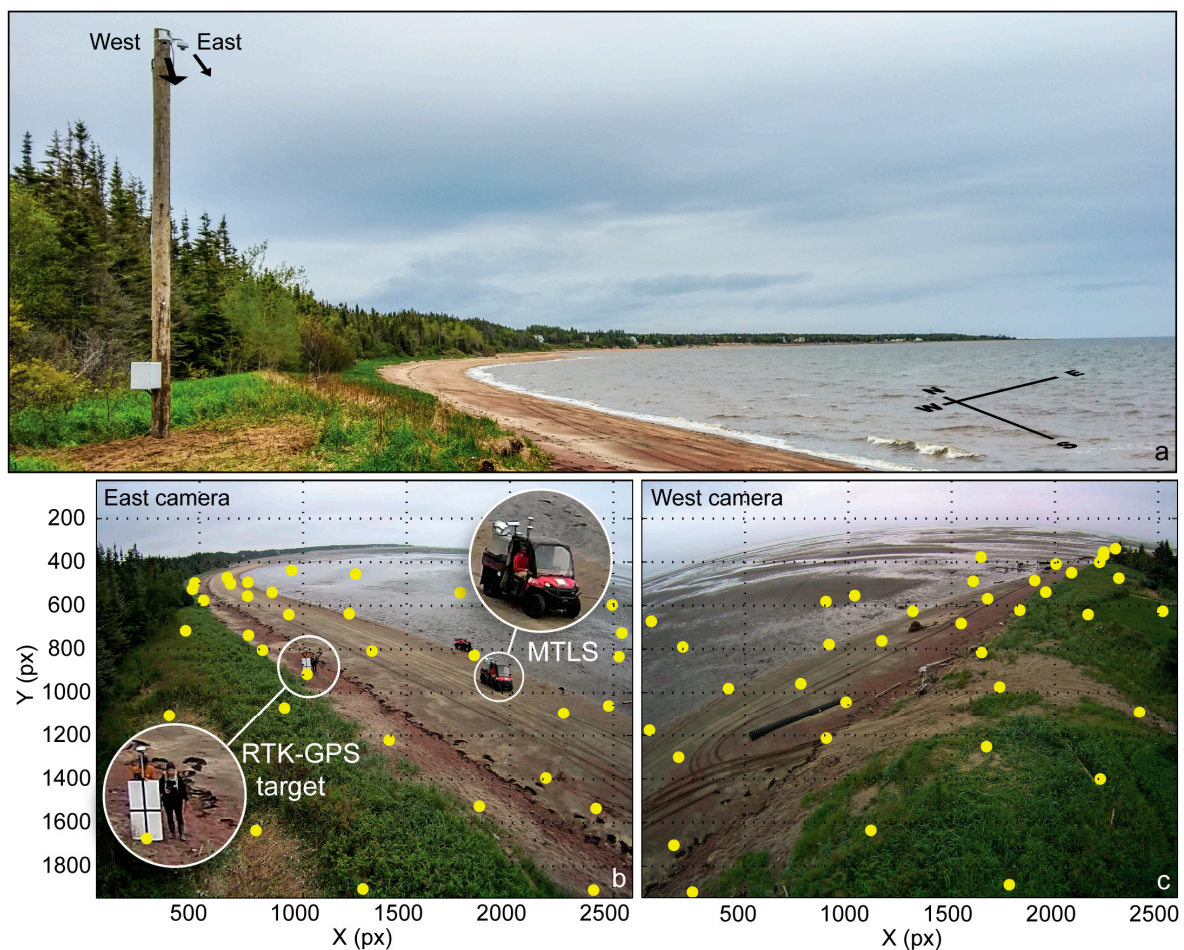


Figure 5. The video camera system of Pointe-Lebel is located at 5 m from the beachface (a). Ground Control Points (GCPs showed as yellow dots) for image to ground coordinate conversions were acquired with RTK–GPS on the beachface and the tidal flat during the LiDAR survey on the east (b) and west side of the beach (c) on 3 August 2016. The GCPs and LiDAR acquisitions are shown in (b).

2.5. Cameras Calibration

Optical measurements are subject to image distortions due to inherent camera characteristics. The calibration process enables an estimation of these parameters, and establishes a mapping conversion model from image to ground coordinates. The technique described in Stumpf et al. [63] was used because of its ability to deal with radial lens distortion and estimations for exterior orientation, focal length, skew factor, and principal point. The calibration requires at least nine ground control points (GCPs) for each camera that cover the entire camera view and that are evenly distributed on the beach and tidal flat at low tide. Only GCPs closer than 230 m from the camera system (yellow dots in Figure 5b,c, east: 33 GCPs; west: 38 GCPs) were used for the calibration in order to minimize the horizontal uncertainty, resulting to final GCP RMSEs of 0.38 and 1.11 m for the west and east cameras, respectively. The mapping algorithm was then used to convert all detected shorelines (pixel coordinates) into ground coordinates.

The alongshore pixel footprint increases with distance from the cameras. Within 230 m, projections of each pixel from camera dimensions to x - y geographical coordinates result in ground pixel footprints of 1 cm \times 1 cm (longshore \times cross-shore) close to the cameras. It increases up to 2.8 m in the alongshore direction while the cross-shore footprint remains under 0.5 m.

2.6. Shoreline Detection and Water Elevation Models

Five-minute video segments were acquired during the rising tide of 3 August 2016 between 12:50 and 16:00 (EST) and on 18 November 2016 between 14:00 and 17:30 (EST). LiDAR surveys were conducted simultaneously with video acquisitions. All image analyses were performed using Matlab. Outputs are 5-min time-averaged images (TIMEX) used for shoreline detections based on the presence of swash at the water/beach junction.

The shoreline detection is applied in two steps [38]. As a first approximation, all shorelines were automatically extracted based on a blue, green and red color ratio ($B + G/R$) on all TIMEX images, where B, G, and R are respectively the pixel intensity values of the blue, green, and red channels. The processing was computed for all pixels in a pre-defined region of interest (ROI) on the beach (Figure 6a). The shoreline represents a local minimum in $B + G/R$ ratios over the entire ROI, with lower ratio values (pixel ratio values <1) corresponding to the beachface while the water surface falls under higher ratios, typically over 1. The next step is the shoreline detection and identification on the TIMEX images. The technique is based on the alongshore shape of the swash on the beach in the ROI and detects the water/land boundary rather than dry/wet sand contours [38]. Falsely detected shorelines due to sunshine reflectance on the water, debris at the shoreline, and people on the beach were discarded, but no manual intervention was applied in the delineation.

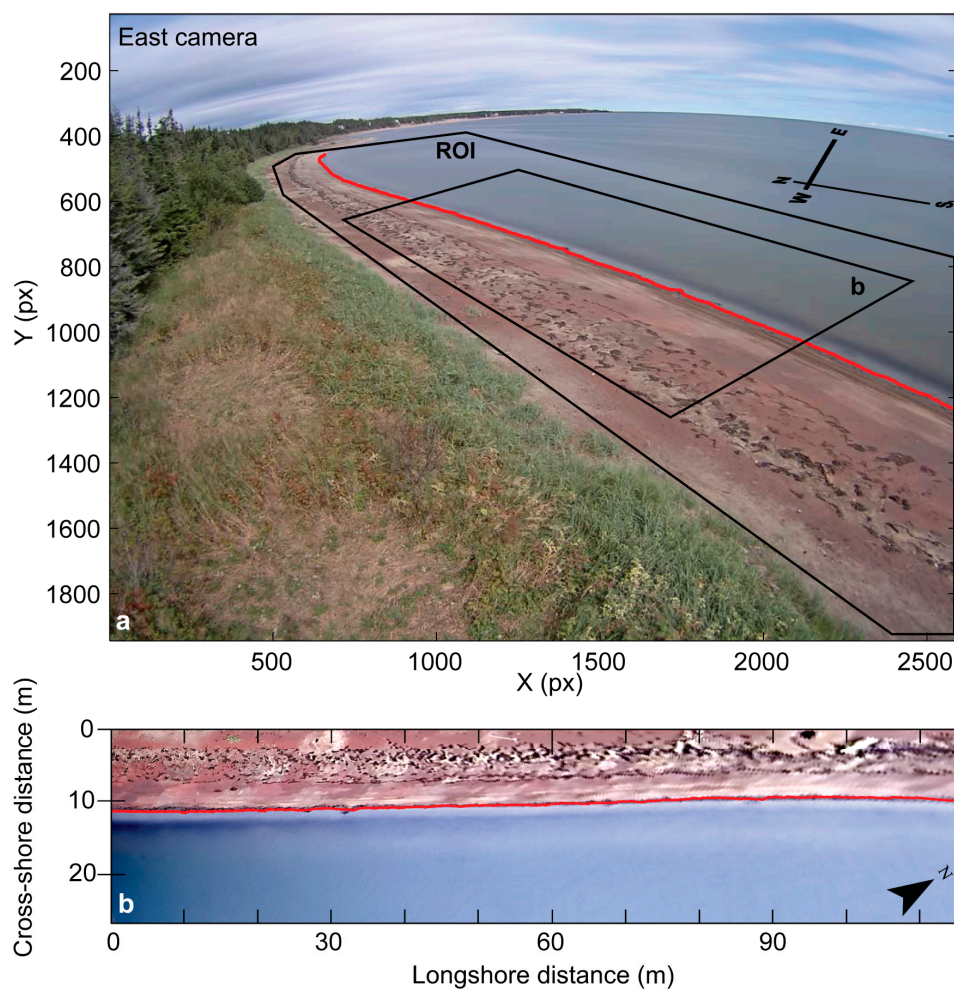


Figure 6. Time-averaged (TIMEX) image with a detected shoreline in calm conditions (red line) (a) and geo-rectified detected shoreline (red line) shown on a time-averaged image from the east camera of Pointe-Lebel (b).

In order to create video-derived digital elevation models (DEMs) from all the image-detected shorelines, a constant alongshore elevation value was first attributed to each detected shoreline [64]. This step generally underlines some assumptions because knowing the exact shoreline elevation in the absence of in-situ water levels and wave time series is not straightforward. The association of water levels to shorelines is normally based on empirical formulations [65]. Here, two different water elevation models (referred to M1 and M2) were tested and associated to the detected shorelines to create two different video-based DEMs. Both water elevation models are associated to observed hydrodynamic parameters at G1 (at the beachface toe). The first model (M1), the image-detected shoreline elevation based on the mean water level Z_{mwl} , is equal to η_{tide} which is the low-frequency still water level (astronomical tide + barometric surge).

The second water elevation model (M2) represents the total water level (TWL) observed at the beach/water line junction (Z_{twl}). It includes the still water level and the wave effect through the significant wave height. All analyses were made during low energy conditions to minimize uncertainties associated with high runup/setup values resulting from wave breaking [65,66]. Given that smaller waves are assumed to generate smaller runup values and therefore result in less detection errors due to swash length than during high energy conditions, the approach was applied during low energy conditions only ($H_s < 0.15$ m). M2 directly uses the nearshore observed significant wave height instead of empirical runup equations based on offshore wave conditions that would obviously increase the overall uncertainty of the approach (e.g., [64,66]). The second model (M2) thus takes the following form:

$$Z_{twl} = \eta_{tide} + H_s \quad (1)$$

The TWL model (M2) is justified by the fact that the Manicouagan peninsula mainly faces small waves outside of storm events, thus enabling the creation of DEMs with a high temporal resolution. We validated this assumption by extracting the occurrence associated to $H_s < 0.15$ m from a WAVEWATCH III (WW3) simulation at 8.3 km offshore, eastward of the study site. WW3 is forced with atmospheric forcing from the Climate Forecast System Reanalysis (CFSR, NCEP/NOAA). Oceanic forcing (currents, water levels, sea ice thickness and concentration) come from a Regional Oceanic Model (ROM) (5 km \times 5 km grid) operated by the Institut des Sciences de la Mer de Rimouski (ISMER). Hourly waves were simulated for the 1980–2009 period at a 5-km grid. Considering the entire 30 yrs time series, offshore waves (H_s) are under 15 cm 58% of the time.

Errors associated with the video-based approach have been assessed. First, the LiDAR elevation associated to the detected shorelines was extracted to compare the overall effectiveness of both water elevation models (Z_{mwl} and Z_{twl}). This analysis enabled a direct comparison between the raw data (image-detected shorelines elevations) and LiDAR points prior to the creation of DEMs. A TIN grid elevation was then created in LP360-QCoherent software from the LiDAR points and from both models of video-based contour lines (M1 and M2). Point clouds were all sampled to a fixed squared 20 cm \times 20 cm mesh grid. The latter was used to create the DEMs with the same pixel resolution of $\Delta x = \Delta y = 20$ cm. For both surveys, the overall surface elevation (z) of the LiDAR-derived matrices were compared to video-based DEMs with linear regression analysis.

The shoreline detection x – y errors were also analysed by extracting a reference contour line (rfl) associated to the mean high tide ($z = 1.19$) from all DEMs. This elevation was chosen because it is prone to be reached on the beach virtually every day, since it represents the mean level of high tides. The cross-shore variability of the rfl was systematically calculated at 5 m alongshore intervals between video-derived models and LiDAR within the same date. Furthermore, the performance of the video system to estimate the temporal shoreline cross-shore net displacements was analyzed. The cross-shore displacements of the rfl between November and August as observed with video cameras (Δy_{vid}) were compared to the displacements observed with the LiDAR system (Δy_{lid}). Finally, in order to analyse the potential of the video system to obtain morphological parameters on the beach in a context of risk management, beachface slopes $\tan \beta_{bf}$, particularly used in runup empirical equations [34] and numerical models [67], were also calculated on these profiles using linear regression over the swash

zone. In this paper, $\tan \beta_{bf}$ was calculated between the maximum water level on the beach and the beachface toe.

3. Results and Discussion

3.1. Shoreline Detection and Elevation Analyses

The video system provided continuous image acquisitions at 4 Hz during daylight on 3 August and 18 November 2016 on the beach of Pointe-Lebel. The image analysis was performed on 5-min TIMEX images during the rising tide while a pressure sensor located at the beach toe synchronously acquired mean water levels and wave characteristics. This setting enabled the extraction of 21 (~83,000 points) to 25 (~98,000 points) contour lines during 3 August and 18 November 2016, respectively. This difference is solely due to a larger tidal amplitude on November 18.

Most studies suggest using a longer averaging period, usually 10 min TIMEX [4,28,36,39,43,65,68] to 15 min [69]. The methodological choice of long period time-averaged images is based on the time period of wave groups and the fact that a longer exposure enables a more complete “storage” of the processes on the beach such as wave breaking [21] that generate foam at the shoreline or over bars. By recording all image intensities at each pixel during this period, commonly used detection techniques such as the SLIM (shoreline intensity maximum), ANN (artificial neural network), PIC (pixel intensity clustering) and CCD (color channel divergence) methods can be applied in most cases [48]. Using colour ratios combined with a pattern recognition algorithm does not necessarily require such long TIMEX durations as noted by Almar et al. [38]. In fact, using shorter time-averaged digital images (<2 min) can overcome some errors that could result from the local swash length on the beach. Although the sensitivity of the detection from varying image-averaging time was not assessed in this paper, 5 min-averaged shoreline detection was considered suitable for the rather steep beachface slope of Pointe-Lebel, thus minimizing possible errors that could arise from the tidal variation over the course of longer time-averaging period [48].

An assessment of the video-derived shoreline vertical accuracies was made. The correlation analysis between detected shoreline points and their correspondence on the LiDAR DEM shows that both shoreline elevation models perform well (Figure 7). With vertical RMS errors of 0.06 m, and high correlation coefficients ($R^2 = 0.99$, p -value <0.001) (Table 1), both linear regressions are well correlated.

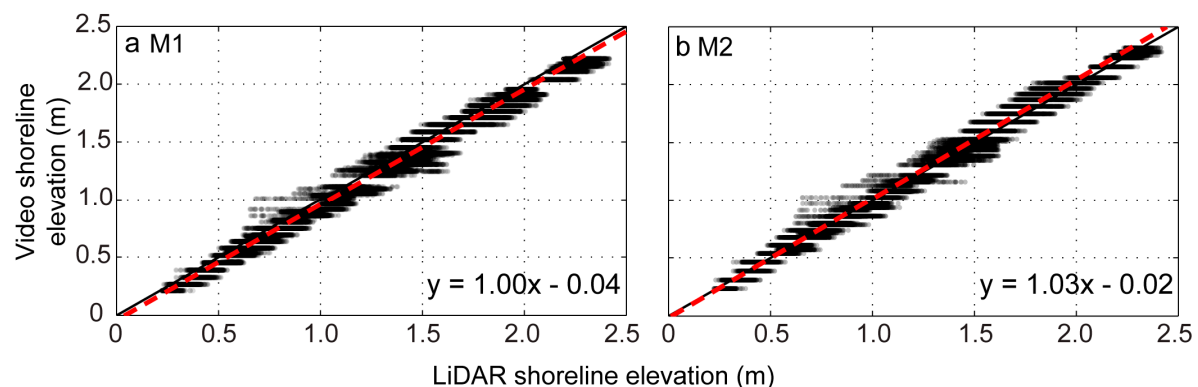


Figure 7. Video-based shoreline elevations versus LiDAR data as parameterized with the shoreline elevation model including only the mean water level (M1) (a) and the total water level (M2) (b). Regression lines are shown by red dashed lines. The black line represents the 1:1 line.

Differences lay mostly on the offset values, with an origin offset of -0.04 for the M1 (mean water level only) and -0.02 m for M2 (total water level), respectively. These results indicate that the overall contribution from H_s is small in the total water level approximation (M2) but it reduces the origin offset by 2 cm. Slopes of both regression lines are very near 1:1, with the coefficient of the M2 being

slightly higher than the M1 (1.03 instead of 1.00). Although the highest wave reached only 0.14 m, this difference can be mainly explained by higher waves at high tide in the M2 model, which is not considered in the mean water level model (M1). Almar et al. [38] noted similar results, indicating a positive and linear relationship between the detection errors and the local swash length, which in return could necessitate a correction factor to reduce uncertainties associated with runup excursions [48]. This suggests that despite a lower origin offset in M2, using the mean water level only (M1) could potentially limit the uncertainty associated with higher wave heights at the beach. Moreover, the slope coefficient of the regression line being precisely 1.00 in M1 suggests that using mean water levels only during low wave conditions provides skillful results along the coast of Pointe-Lebel, as also noted by Morris et al. [45] in calm conditions on a tidal flat.

3.2. Comparing Video- to LiDAR-Based Topography

Digital elevation models were created from video-detected shorelines and LiDAR cloud points on the same $20\text{ cm} \times 20\text{ cm}$ meshgrid for both surveys. Both shoreline elevation models (from video) performed well in predicting the beachface shoreline elevations (Figure 7), and such correspondence is also found on the resulting DEMs (results from August are shown as an example, Figure 8). With the integration of H_s and the mean water level, M2 offers a more accurate morphology of the beachface compared to M1. The sediment accumulation on the west part of the beach, clearly visible with the LiDAR survey, is more perceived with M2 although it is still present on the DEM produced with M1. Differences between video- and LiDAR-based topography were calculated to obtain a differential DEM in the ROI (Figures 9 and 10). As shown in Figure 9a,b, the sediment accumulation on the west part of the beach is explained by anthropogenic debris (hard plastic pipe drain) acting as an artificial tombolo. The reference line of the mean high tides ($z = 1.19\text{ m}$) was extracted from the 3 August survey (from each raster) and is presented to give an overview of the erosion that occurred between the surveys.

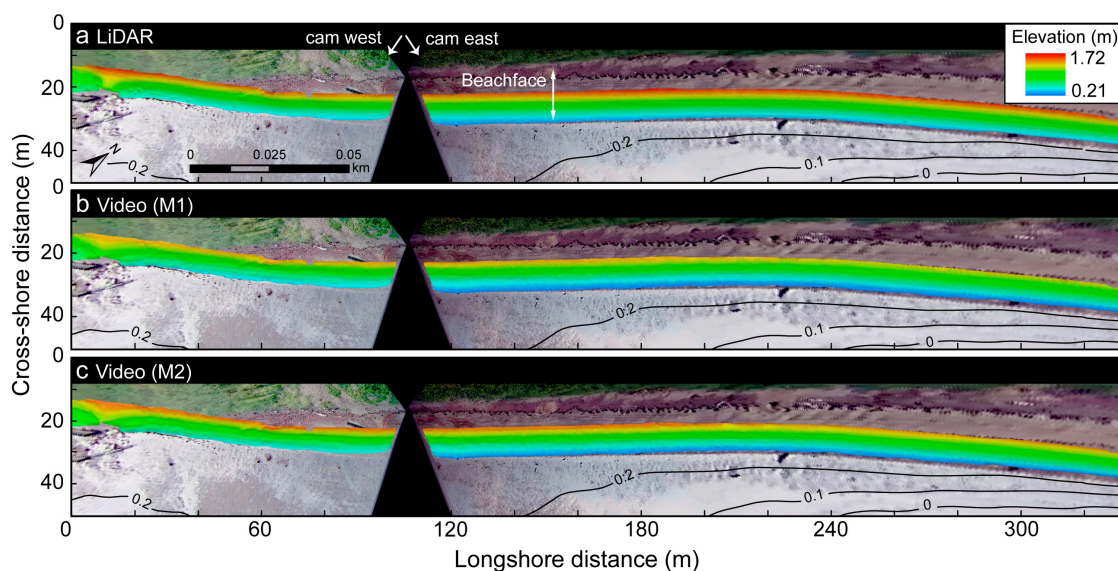


Figure 8. Beachface topography of 3 August 2016 obtained from LiDAR (a) and video imagery as defined with (b) the shoreline elevation model 1 (M1, Z_{mwl}) and (c) model 2 (M2, Z_{twl}).

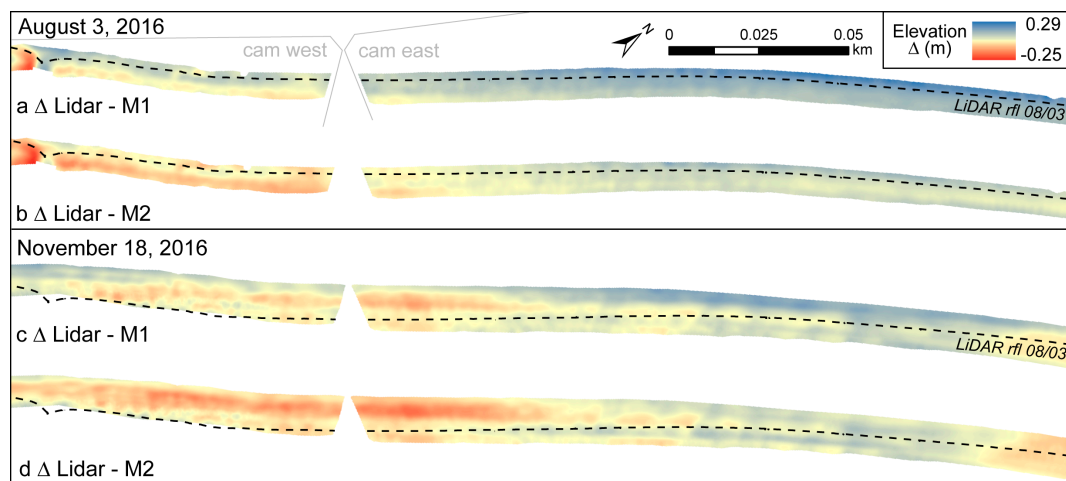


Figure 9. Overall differences between the LiDAR surveys and the video-based topography for 3 August (a,b) and 18 November (c,d). The 1.19 m *rfl* of 3 August as extracted from the LiDAR is shown on all figures.

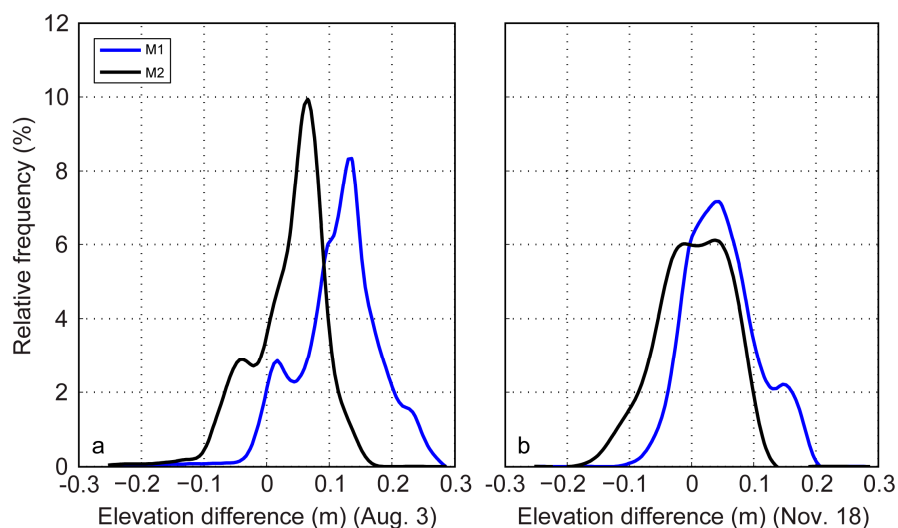


Figure 10. Relative frequency (%) of the Δ LiDAR- Z_{mwl} (M1) and Δ LiDAR- Z_{twl} (M2) digital elevation models' (DEMs) differences (over all pixels) as observed during 3 August (a) and 18 November (b). Positive values indicate higher elevations on the LiDAR and underestimations by the shoreline detection model.

The sediment accumulation located on the west camera view (left side of Figure 9a,b) creates a shadow zone preventing the west camera to precisely locate the shorelines. This promotes rogue detections and therefore increased elevation uncertainties at this location. On Figure 9c,d, this sediment accumulation is no longer in place due to the beach's response to a storm event that occurred on 16 November. As a result of sediment transport, the video-derived topography at this location is well predicted in November (Figure 9c,d).

The cameras in Pointe-Lebel being located at only 12 m above mean sea level, all analyses are limited to 230 m from each camera to keep planimetric errors lower than ~ 1 m. Within this distance, despite the shadow zone mentioned above, overall video-derived DEM elevation differences all range between -0.25 m and 0.29 m. Spatial coverage depends on the camera elevation [21]. These errors could therefore be overcome by elevating the cameras, as in previous works (e.g., McCarroll et al. [70]

(55 m), Bracs et al. [65] (44 m), Sénéchal et al. [32], Almar et al. [38] (27 m), Vousdoukas et al. [47] (20 m), Abessolo Ondo et al. [69] (15 m)).

According to the entire relative frequency of the elevation difference between the LiDAR and the video-derived DEMs (Figure 10), the worst model for each survey date is systematically M1 with a mean underestimation of 0.12 m (3 August) and 0.05 m (18 November), although M2 still underestimates the mean ground elevation by 0.04 m during 3 August. The best elevation model remains M2, especially on November 18 with a bias equal to zero and a standard deviation of 0.06 m (Figure 10b).

This range of uncertainty corresponds well to previous conclusions. Vousdoukas et al. [47] obtained vertical RMS errors of 0.26 m using empirical formulations based on tidal and wave runup levels on the beach. Similarly, Uunk et al. [36] mentioned elevation RMS errors between 0.28 and 0.34 m, the highest values being observed with a completely automated method. These uncertainties may in fact result from the underlying empirical relationships relating shoreline elevations to offshore wave characteristics and water levels [42]. Instead of assuming empirical relationships to estimate the shoreline elevations, the similar approach applied here uses in-situ water levels and only small wave heights (<0.15 m). Similarly, Blossier et al. [71] selected only wave heights less than 1 m to minimize errors associated with wave setup estimations. Errors obtained above are thus in the range of what was observed by Morris et al. [45], whom by using DGPS-RTK for shoreline validations in a lagoon without wave effects, obtained vertical accuracy in the order of 0.05 m. The results presented here validate the video-derived elevation values with the LiDAR topographic surveys. The LiDAR cloudpoint with a high precision (± 0.03 m) acts as a benchmark topography, providing validation points virtually everywhere on the beachface. Using M2 to produce a beachface DEM gives an estimation of the morphology as skillful as the one acquired with the LiDAR survey.

3.3. Cross-Shore Position of the Shoreline

To further investigate the performance of the video-based DEMs, a cross-shore analysis of shoreline migrations was made. Such shoreline extraction technique is often used to establish long-term morphodynamic patterns and has been proven to outperform common beach monitoring strategies (e.g., RTK-GPS profiles, aerial LiDAR surveys) mostly because advantages provided by the low costs and the high spatiotemporal resolution overcome disadvantages of the limited coverage [10]. Contrary to other techniques however, the estimation of shoreline elevations and their cross-shore position systematically comes with some planimetric uncertainties that can reach many meters [66].

For each DEM, the mean high tide reference line (1.19 m, noted *rfl*) was extracted and smoothed using a 5 m alongshore window to filter the smallest features on the beach such as algae and wood debris. Its location between video- and LiDAR-based DEMs on a given date was first evaluated at 65 cross-shore profiles with an alongshore spacing of 5 m. As observed on Figure 11, cross-shore locations of the *rfl* along the beach of Pointe-Lebel spanned between ~6 m and ~11.5 m from the land. Cross-shore locations of the *rfl* are well-correlated between LiDAR and video-derived beachface DEMs. With a correlation coefficient $R^2 = 0.95$ (Table 1), and a root-mean-square error of 0.27 m, M2 performs better than M1 ($R^2 = 0.81$, RMSE = 0.52 m). Furthermore, the mean deviation (MD) obtained with M2 (0.31 m) is at least half the value of M1 (0.63 m).

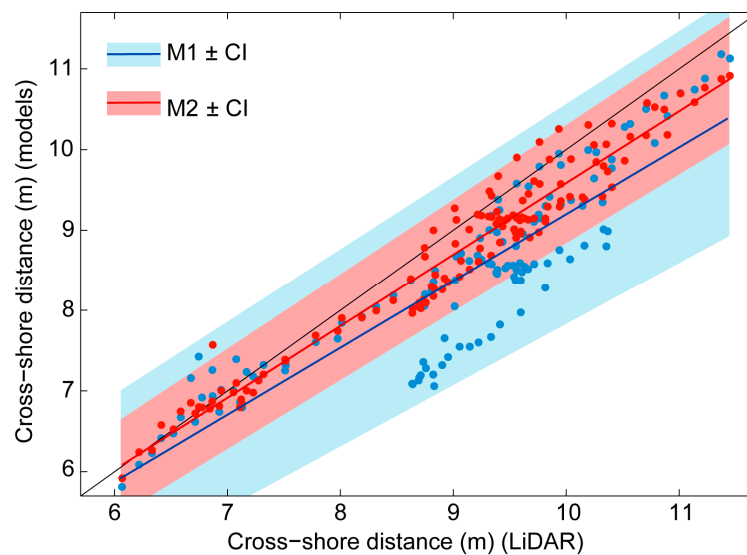


Figure 11. Regression analysis of the cross-shore locations of the shoreline (rf) between each video shoreline elevation model and LiDAR data (M1: blue. M2: red.; \pm confidence intervals (CI)). The black line represents the 1:1 line.

Table 1. Regression analysis results and skills for the shoreline elevation models according to the evaluated morphological metrics (MD: mean deviation; MAD: mean absolute deviation).

| Analysis | Model Fit | Model Skill | | | | |
|--|-----------|-----------------|------|-------|-------|-------|
| | | R^2 | RMSE | MD | MAD | |
| Shoreline detection (Δz) | M1~LiDAR | $1.00x - 0.04$ | 0.99 | 0.06 | -0.04 | 0.06 |
| | M2~LiDAR | $1.03x - 0.02$ | 0.99 | 0.06 | 0.02 | 0.05 |
| Cross-shore location (Δy) (same date) | M1~LiDAR | $0.83x + 0.90$ | 0.81 | 0.52 | 0.63 | 0.66 |
| | M2~LiDAR | $0.89x + 0.68$ | 0.95 | 0.27 | 0.31 | 0.36 |
| Cross-shore displacements (Δy) (multi-dates) | M1~LiDAR | $1.11x + 0.92$ | 0.97 | 0.35 | 0.83 | 0.85 |
| | M2~LiDAR | $1.02x + 0.12$ | 0.97 | 0.33 | 0.11 | 0.24 |
| Beachface slopes ($\Delta \tan \beta_{bf}$) (August) | M1~LiDAR | $0.95x + 0.006$ | 0.73 | 0.007 | | 0.014 |
| | M2~LiDAR | $0.99x - 0.007$ | 0.79 | 0.006 | | 0.008 |
| (November) | M1~LiDAR | $0.64x + 0.04$ | 0.39 | 0.005 | | 0.007 |
| | M2~LiDAR | $1.02x$ | 0.66 | 0.004 | | 0.004 |

3.4. Spatiotemporal Analysis of the Morphological Evolution

The cross-shore shoreline displacement over time has also been assessed on the beach of Pointe-Lebel (Figure 12). Significant shoreline displacements were observed between 3 August and 18 November 2016 with the LiDAR surveys. The net onshore shoreline displacement (with a maximum erosion of -3.77 m) observed with LiDAR is located within the west camera view (Figure 12a). On the east view, the LiDAR shows a rather different trend where a net displacement (-2.78 m) close to the camera (y location: 2517080895 m) is compensated by a net seaward displacement peaking at $+1.30$ m (y location: 2518150266 m). Same trends are observed with both video-based models, but the maximum erosion/advance observed at these same longshore locations are -3.56 m/ $+2.70$ m and -3.69 m/ $+1.55$ m with the M1 and M2, respectively.

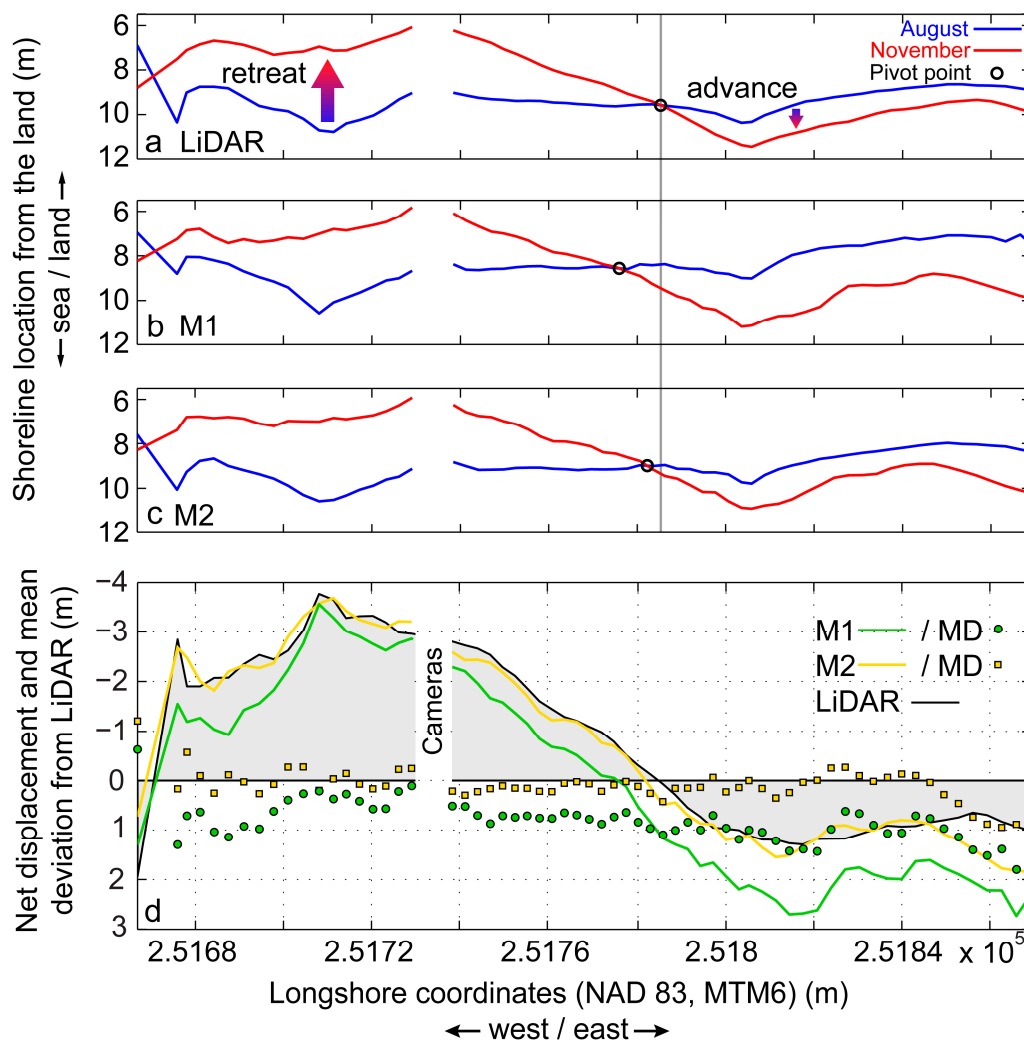


Figure 12. Longshore variation of the cross-shore position of the reference shoreline (1.19 m elevation contour) obtained during the surveys. The patterns of erosion/advance observed with the LiDAR surveys (a) are also distinguished with both M1 (b) and M2 (c), but the net displacement (d) is best fitted by the M2 model (yellow curve, panel d). Dots show the mean deviation (MD) of the data. The pivotal point of the beach as detected with M2 is closely located to the smoothing window size (~5.25 m) (black circles, panels a–c).

Both models skillfully predict shoreline displacement behaviors ($R^2 = 0.97$) (Table 1), and the results are virtually the same. M2 lowers to 0.33 m the planimetric RMSE compared to M1 (RMSE = 0.35 m) and the regression line is closer to 1:1 with a lower origin offset ($1.02x + 0.12$). As observed from the assessment of cross-shore positions (Figure 11), M2 indicates a net displacement that is closer (0.11 m) to the original displacement observed on LiDAR (compared to observations from M1). The latter indicates a quasi-systematically biased displacement of 0.83 m toward the water (Figure 12d, green line), a result inherent to the mean water elevation association to the shoreline. Integrating the RMS errors associated with the cross-shore location only (Section 3.4), total RMSE are still under 1 m for both M1 (0.87 m) and M2 (0.60 m). The shoreline elevation model M2 thus shows a closer relationship between the real displacements observed on the beach with the LiDAR, and further agrees with the conclusions of Aarninkhof et al. [42], stating that their detection technique (the Hue-Saturation-Value (HSV) method) identifies a shoreline at the higher end of the runup excursion. As also noted above, the results presented here using the Almar's shoreline

detection technique [38] justify the integration of waves as a proxy to runup into the shoreline elevation estimation.

The comparison of the reference shoreline's alongshore position between the LiDAR surveys over time shows a rotation pattern on the beach of Pointe-Lebel (Figure 12). Such beach dynamic is the result of both beach extremities showing contrasting behaviors: erosion on one side and advance on the other [71]. This rotation could be related to the storms that occurred on 22 October and from 12 to 16 November, the latter occurring two days before the second survey. Although no wave directions data in the nearshore zone could be related to the dynamic beach response, the offshore wave directions were mainly from the south and ranged from 100° (22 October, 16 November) to 230° (12 November). The pressure sensor G1 recorded wave heights reaching 0.98 m at the beach toe during the 2.79 m high tide on 16 November (14:36 EST) (Figure 3). These events caused major erosion on the beach.

Previous studies have shown the efficiency of video monitoring stations to quantify beach rotations due to sediment transport processes [68] or beach exposure to wave directions [64]. A pivotal point is indicated by a local minimum in the displacement of the shoreline [68]. Indeed, the high frequency image acquisition enabled the observation of the beach's pivotal rotation point both with M1 and M2 shoreline elevation models (Figure 12b,c). Extracted shorelines with M1 indicate the pivotal point's location at 17.18 m westward of the LiDAR-derived point. The distance is much improved with M2, being located at 5.25 m from the real central rotation point observed on the LiDAR. This is in fact within a close range of the longshore averaged shoreline 5-m window.

Beachface slopes were also calculated from regression analysis over the 65 cross-shore profiles along the beach from video- and LiDAR-based DEMs for both surveys (Figure 13). For the 3 August survey, beachface slopes obtained from LiDAR have scattered values, showing a left-skewed distribution ranging between 0.082 and 0.164, with an average of 0.142. These values are typically associated with steep slopes of reflective beachfaces [72]. Slopes calculated from M1 and M2 are well-correlated to the LiDAR-derived beach slopes (Table 1), with $RMSE \leq 0.007$ for both models and R^2 of 0.73 and 0.79 for M1 and M2, respectively. However, during the November survey, regression trends are less defined. Furthermore, the average beachface slope is slightly lower in November (0.124) with values ranging from 0.116 to 0.144. Indeed, this is the result of net erosion and sediment transport that occurred on November 16 on the upper beach. The optimal model is M2, with $RMSE = 0.004$, and the correlation is strong ($y = 1.02x$, $R^2 = 0.66$). The regression is however not significant with M1, and beach slopes are thus not well correlated. It appears to be the result of underestimations of shoreline elevations with M1 near the high tide on 18 November, giving smaller beachface slope values. This observation is also noted on the August survey.

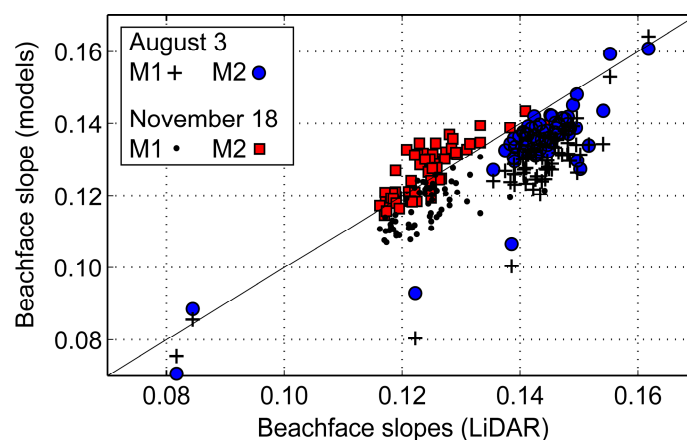


Figure 13. Longshore variability in beachface slopes between video-based models and LiDAR-based DEMs. The black line is the 1:1 line.

3.5. Perspectives and Limitations

Compared to a LiDAR survey, the video-derived DEM technique is less time-consuming and more cost-effective. In low energy coastal environments such as the St. Lawrence Estuary, the technique makes it possible to exclude any uncertainties that are commonly induced by empirical setup/runup relationships. It however implies some inherent centimeter-scale elevation uncertainties based on the sensor's technical accuracy (manufacturer-specified accuracy: ± 5 mm of water depth) and mostly its vertical positioning with RTK-GPS. Moreover, with the second model (M2), one needs to obtain H_s at the beachface toe during low energy events. Interestingly though, on Pointe-Lebel beach, it is possible to apply this remote sensing technique 58% of the time (i.e., under such low conditions), including during winter when it is not always possible to access the beach with other monitoring strategies because of snow and sea ice. The possibility to acquire a beach topography with a high temporal frequency could potentially highlight coastal processes occurring during winter season, while land fast ice is under constant modification in response to climate change. Although there is high confidence of a progressive disappearance of sea ice toward 2100 in the Gulf of the St. Lawrence [56], more field data acquired with video stations on the dynamics of coastal sea ice in the St. Lawrence Estuary could provide more knowledge on the impact of climate change in sub-arctic estuaries. On more energetic coasts, higher values of H_s could increase the errors of this model (M2) and could prevent us from applying the method. In such a case, further sensitive analysis of the M2 results as a function of an increase in H_s would need to be made.

Contrary to LiDAR surveys, the video-based technique is limited to the maximum extension of the tidal range during the survey (i.e., from the lowest to the highest elevation shorelines detected). Furthermore, the automatic extraction technique applied here, which undertakes a water/beach distinction from color band ratios and a shoreline shape recognition module [38], failed at low tide mainly because the water depth was too shallow, therefore limiting swash detection and promoting numerous rogue detections of the sandy bottom. Vousdoukas et al. [47] mentioned that rogue detections could be observed under high wave conditions, therefore promoting some rogue automated detections. Erroneously identified shorelines in our study were rather the result of calm conditions during low tide. The technique applied on the steep beachface and dissipative tidal flat of Pointe-Lebel would therefore need to be improved for shoreline detections at low tide, or could be combined with a manual detection to minimize the errors [66] while the water depth is especially low and the sandy bottom is visible. Such optical conditions prevent the discretization between the water and the beach.

4. Conclusions

A shoreline detection technique from a low-cost video monitoring station was used to create digital elevation models (DEMs) of a steep beachface on a tidal flat at two different dates. Environmental conditions were calm during both surveys, with nearshore wave heights less than 15 cm. Two shoreline elevation models were tested against LiDAR-derived shorelines and interpolated topography. The first model is the simplest and the elevation is only associated to the mean water level recorded at the beach toe. Although it performs relatively well to predict the shoreline position and elevation, this model generally underestimates individual shoreline elevations by roughly 4 cm, and cross-shore positions errors are in the order of 0.63 m (MD) toward the sea. Although it is within an acceptable planimetric uncertainty ($\Delta x, \Delta y < 1$ m) for spatiotemporal shoreline migration assessments, a correction factor needs to be applied to palliate this issue, therefore the method is not necessarily an improvement over previous studies. The shoreline model including the effect of runup, integrated here as a proxy via direct measures of waves at the beachface toe, performs better both in terms of overall vertical (Δz) and planimetric uncertainties ($\Delta x, \Delta y$), respectively < 6 cm and < 31 cm (MD). This approach greatly facilitates the acquisition of continuous coastal topographic observations that is virtually as effective as a LiDAR survey, because it is not based on an estimation of wave-induced setup or runup that would imply some uncertainties in the shoreline location and elevation. A digital elevation model is usually necessary in geomorphological analysis in coastal studies and management. This study

presented a video-based technique for the creation of DEMs that covers the range of video-detected shorelines during a tidal cycle, offering similar skills to a LiDAR-based raster surface with total elevation errors under 11 cm. Therefore, the approach enables a precise measurement of morphological parameters used in geomorphology and coastal engineering (e.g., shoreline displacement, beach slope, DEM, sediment budget) while remaining an accessible approach for professionals responsible for coastal risk management.

Acknowledgments: The authors thank the Québec Ministry of Public Security for funding the project. D. Didier received a scholarship from the Fonds Québécois de la recherche sur la nature et les technologies. The project would not have been possible without the research assistants from the LDGIZC (Canada) and LGO (France). The authors greatly acknowledge the coastal citizens of Pointe-Label for their support and constant surveillance of the video station. We would like to acknowledge five anonymous reviewers for their helpful suggestions and comments.

Author Contributions: D. Didier, P.B., E.A., D. Dumont and C.D. designed the research project; D. Didier and P.B. installed the video station; E.A., C.C., D. Didier and F.F. contributed to the image analysis tools; D. Didier, E.A., E.B., L.C. processed/analyzed the data. D. Didier, P.B., E.A., C.C. and D. Dumont wrote the paper.

Conflicts of Interest: The authors declare no conflict of interest. The founding sponsors had no role in the design of the study; in the collection, analyses, or interpretation of data; in the writing of the manuscript, and in the decision to publish the results.

References

1. Masselink, G.; Puleo, J.A. Swash-zone morphodynamics. *Cont. Shelf Res.* **2006**, *26*, 661–680. [[CrossRef](#)]
2. Ruessink, B.G.; Kleinhan, M.G.; van den Beukel, P.G.L. Observations of swash under highly dissipative conditions. *J. Geophys. Res. Oceans* **1998**, *103*, 3111–3118. [[CrossRef](#)]
3. Sous, D.; Petitjean, L.; Bouchette, F.; Rey, V.; Meulé, S.; Sabatier, F.; Martins, K. Field evidence of swash groundwater circulation in the microtidal rousty beach, France. *Adv. Water Resour.* **2016**, *97*, 144–155. [[CrossRef](#)]
4. Huisman, C.E.; Bryan, K.R.; Coco, G.; Ruessink, B.G. The use of video imagery to analyse groundwater and shoreline dynamics on a dissipative beach. *Cont. Shelf Res.* **2011**, *31*, 1728–1738. [[CrossRef](#)]
5. Vousedoukas, M.I.; Velegrakis, A.F.; Dimou, K.; Zervakis, V.; Conley, D.C. Wave run-up observations in microtidal, sediment-starved pocket beaches of the Eastern Mediterranean. *J. Mar. Syst.* **2009**, *78*, S37–S47. [[CrossRef](#)]
6. Yates, M.L.; Guza, R.T.; O'Reilly, W.C. Equilibrium shoreline response: Observations and modeling. *J. Geophys. Res.* **2009**, *114*, C09014. [[CrossRef](#)]
7. Hardisty, J. A morphodynamic model for beach gradients. *Earth Surf. Process. Landf.* **1986**, *11*, 327–333. [[CrossRef](#)]
8. Aagaard, T.; Black, K.P.; Greenwood, B. Cross-shore suspended sediment transport in the surf zone: A field-based parameterization. *Mar. Geol.* **2002**, *185*, 283–302. [[CrossRef](#)]
9. Forbes, D.L.; Taylor, R.B. Ice in the shore zone and the geomorphology of cold coasts. *Prog. Phys. Geogr.* **1994**, *18*, 59–89. [[CrossRef](#)]
10. Blossier, B.; Bryan, K.R.; Daly, C.J.; Winter, C. Spatial and temporal scales of shoreline morphodynamics derived from video camera observations for the island of Sylt, German Wadden Sea. *Geo-Mar. Lett.* **2016**. [[CrossRef](#)]
11. Bernatchez, P.; Fraser, C. Evolution of coastal defence structures and consequences for beach width trends, Québec, Canada. *J. Coast. Res.* **2012**, *285*, 1550–1566. [[CrossRef](#)]
12. Trenhaile, A.S. Modeling the accumulation and dynamics of beaches on shore platforms. *Mar. Geol.* **2004**, *206*, 55–72. [[CrossRef](#)]
13. Didier, D.; Bernatchez, P.; Marie, G.; Boucher-Brossard, G. Wave runup estimations on platform-beaches for coastal flood hazard assessment. *Nat. Hazards* **2016**, *83*, 1143–1467. [[CrossRef](#)]
14. Floc'h, F.; Le Dantec, N.; Lemos, C.; Cancouët, R.; Sous, D.; Petitjean, L.; Bouchette, F.; Ardhuin, F.; Suanez, S.; Delacourt, C. Morphological response of a macrotidal embayed beach, Porsmilin, France. *J. Coast. Res.* **2016**, *75*, 373–377. [[CrossRef](#)]
15. Tribbia, J.; Moser, S.C. More than information: what coastal managers need to plan for climate change. *Environ. Sci. Policy* **2008**, *11*, 315–328. [[CrossRef](#)]

16. List, J.H.; Farris, A.S.; Sullivan, C. Reversing storm hotspots on sandy beaches: Spatial and temporal characteristics. *Mar. Geol.* **2006**, *226*, 261–279. [[CrossRef](#)]
17. Cheng, J.; Wang, P.; Guo, Q. Measuring beach profiles along a low-wave energy microtidal coast, West-Central Florida, USA. *Geosciences* **2016**, *6*, 44. [[CrossRef](#)]
18. Coco, G.; Senechal, N.; Rejas, A.; Bryan, K.R.; Capo, S.; Parisot, J.P.; Brown, J.A.; Macmahan, J.H.M. Beach response to a sequence of extreme storms. *Geomorphology* **2014**, *204*, 493–501. [[CrossRef](#)]
19. Silveira, T.M.; Carapuço, A.M.; Sousa, H.; Taborda, R.; Psuty, N.P. Optimizing beach topographical field surveys: Matching the effort with the objectives. *J. Coast. Res.* **2013**, *1*, 588–593. [[CrossRef](#)]
20. Suanez, S.; Cancouët, R.; Floc’h, F.; Blaise, E.; Ardhuin, F.; Filipot, J.-F.; Cariolet, J.-M.; Delacourt, C. Observations and predictions of wave runup, extreme water levels, and medium-term dune erosion during storm conditions. *J. Mar. Sci. Eng.* **2015**, *3*, 674–698. [[CrossRef](#)]
21. McNinch, J.E. Bar and swash imaging radar (BASIR): A mobile X-band radar designed for mapping nearshore sand bars and swash-defined shorelines over large distances. *J. Coast. Res.* **2007**, *231*, 59–74. [[CrossRef](#)]
22. Casella, E.; Rovere, A.; Pedroncini, A.; Mucerino, L.; Casella, M.; Cusati, L.A.; Vacchi, M.; Ferrari, M.; Firpo, M. Study of wave runup using numerical models and low-altitude aerial photogrammetry: A tool for coastal management. *Estuar. Coast. Shelf Sci.* **2014**, *149*, 160–167. [[CrossRef](#)]
23. Mancini, F.; Dubbini, M.; Gattelli, M.; Stecchi, F.; Fabbri, S.; Gabbianelli, G. Using unmanned aerial vehicles (uav) for high-resolution reconstruction of topography: The structure from motion approach on coastal environments. *Remote Sens.* **2013**, *5*, 6880–6898. [[CrossRef](#)]
24. Holman, R.A.; Brodie, K.L.; Spore, N.J. Surf zone characterization using a small quadcopter: Technical issues and procedures. *IEEE Trans. Geosci. Remote Sens.* **2017**, *55*, 2017–2027. [[CrossRef](#)]
25. Vousedoukas, M.I.; Kirupakaramoorthy, T.; Oumeraci, H.; de la Torre, M.; Wübbold, F.; Wagner, B.; Schimmels, S. The role of combined laser scanning and video techniques in monitoring wave-by-wave swash zone processes. *Coast. Eng.* **2014**, *83*, 150–165. [[CrossRef](#)]
26. Blenkinsopp, C.E.; Mole, M.A.; Turner, I.L.; Peirson, W.L. Measurements of the time-varying free-surface profile across the swash zone obtained using an industrial LIDAR. *Coast. Eng.* **2010**, *57*, 1059–1065. [[CrossRef](#)]
27. Brodie, K.L.; Raubenheimer, B.; Elgar, S.; Slocum, R.K.; McNinch, J.E. Lidar and pressure measurements of inner-surfzone waves and setup. *J. Atmos. Ocean. Technol.* **2015**, *32*, 1945–1959. [[CrossRef](#)]
28. Holman, R.; Stanley, J. The history and technical capabilities of Argus. *Coast. Eng.* **2007**, *54*, 477–491. [[CrossRef](#)]
29. Pitman, S.J. Methods for field measurement and remote sensing of the swash zone. In *Geomorphological Techniques*; Cook, S.J., Clark, L.E., Nield, J.M., Eds.; British Society of Geomorphology: Oxford, UK, 2014; Volume 3, pp. 1–14.
30. Almar, R.; Ibaceta, R.; Blenkinsopp, C.; Catalan, P.; Cienfuegos, R.; Trung Viet, N.; Hai Thuan, D.; Van Uu, D.; Lefebvre, J.-P.; Sowah Laryea, W.; et al. Swash-based wave energy reflection on natural beaches. *Proc. Coast. Sediments* **2015**, 1–13. [[CrossRef](#)]
31. Simarro, G.; Guedes, R.M.C.; Sancho, A.; Guillen, J.; Bryan, K.R.; Coco, G. On the use of variance images for runup and shoreline detection. *Coast. Eng.* **2015**, *99*, 136–147. [[CrossRef](#)]
32. Senechal, N.; Coco, G.; Bryan, K.R.; Holman, R.A. Wave runup during extreme storm conditions. *J. Geophys. Res.* **2011**, *116*, C07032. [[CrossRef](#)]
33. Stockdon, H.F.; Thompson, D.M.; Plant, N.G.; Long, J.W. Evaluation of wave runup predictions from numerical and parametric models. *Coast. Eng.* **2014**, *92*, 1–11. [[CrossRef](#)]
34. Stockdon, H.; Holman, R.; Howd, P.; Sallenger, A. Empirical parameterization of setup, swash, and runup. *Coast. Eng.* **2006**, *53*, 573–588. [[CrossRef](#)]
35. Vousedoukas, M.I.; Ferreira, Ó.; Almeida, L.P.; Pacheco, A. Toward reliable storm-hazard forecasts: XBeach calibration and its potential application in an operational early-warning system. *Ocean Dyn.* **2012**, *62*, 1001–1015. [[CrossRef](#)]
36. Uunk, L.; Wijnberg, K.M.; Morelissen, R. Automated mapping of the intertidal beach bathymetry from video images. *Coast. Eng.* **2010**, *57*, 461–469. [[CrossRef](#)]
37. Almar, R.; Senechal, N.; Coco, G. Estimation vidéo haute fréquence de la topographie inter-tidale d’une plage sableuse: Application à la caractérisation des seuils d’engrèvement et d’érosion. In *Xèmes Journées Nationales Génie Côtier—Génie Civil*; Paralia: Sophia Antipolis, France, 2008; pp. 505–514.

38. Almar, R.; Ranasinghe, R.; Sénéchal, N.; Bonneton, P.; Roelvink, D.J.A.; Bryan, K.R.; Marieu, V.; Parisot, J.-P.; Senechal, N.; Bonneton, P.; et al. Video-based detection of shorelines at complex meso-macro tidal beaches. *J. Coast. Res.* **2012**, *28*, 1040–1048. [[CrossRef](#)]
39. Pearre, N.S.; Puleo, J.A. Quantifying seasonal shoreline variability at Rehoboth Beach, Delaware, using automated imaging techniques. *J. Coast. Res.* **2009**, *254*, 900–914. [[CrossRef](#)]
40. Holman, R.; Sallenger, A.; Lippmann, T.; Haines, J. The application of video image processing to the study of nearshore processes. *Oceanography* **1993**, *6*, 78–85. [[CrossRef](#)]
41. Bernatchez, P.; Dubois, J.-M.M. Seasonal quantification of coastal processes and cliff erosion on fine sediment shorelines in a cold temperate climate, north shore of the St. Lawrence maritime estuary, Québec. *J. Coast. Res.* **2008**, *1*, 169–180. [[CrossRef](#)]
42. Aarninkhof, S.G.J.; Turner, I.L.; Dronkers, T.D.T.; Caljouw, M.; Nipius, L. A video-based technique for mapping intertidal beach bathymetry. *Coast. Eng.* **2003**, *49*, 275–289. [[CrossRef](#)]
43. Plant, N.G.; Holman, R. A. Intertidal beach profile estimation using video images. *Mar. Geol.* **1997**, *140*, 1–24. [[CrossRef](#)]
44. Madsen, A.J.; Plant, N.G. Intertidal beach slope predictions compared to field data. *Mar. Geol.* **2001**, *173*, 121–139. [[CrossRef](#)]
45. Morris, B.D.; Coco, G.; Bryan, K.R.; Turner, I.L.; Street, K.; Vale, M. Video-derived mapping of estuarine evolution. *J. Coast. Res.* **2007**, *2007*, 410–414.
46. Turner, I.L.; Leyden, V.M. *System Description and Analysis of Shoreline Change: August 1999–February 2000. Report 1. Northern Gold Coast Coastal Imaging System*; Water Research Laboratory: Manly Vale, NSW, Australia, 2000.
47. Voudoukas, M.I.; Ferreira, P.M.; Almeida, L.P.; Dodet, G.; Psaros, F.; Andriolo, U.; Taborda, R.; Silva, A.N.; Ruano, A.; Ferreira, Ó.M. Performance of intertidal topography video monitoring of a meso-tidal reflective beach in South Portugal. *Ocean Dyn.* **2011**, *61*, 1521–1540. [[CrossRef](#)]
48. Plant, N.G.; Aarninkhof, S.G.J.; Turner, I.L.; Kingston, K.S. The performance of shoreline detection models applied to video imagery. *J. Coast. Res.* **2007**, *23*, 658–670. [[CrossRef](#)]
49. Cariolet, J.-M.; Suanez, S. Runup estimations on a macrotidal sandy beach. *Coast. Eng.* **2013**, *74*, 11–18. [[CrossRef](#)]
50. Melby, J.; Caraballo-Nadal, N.; Kobayashi, N. Wave runup prediction for flood mapping. In Proceedings of the Coastal Engineering, Santander, Spain, 1–6 July 2012; Volume 1, p. 79.
51. Bernatchez, P.; Dubois, J.-M.M. Bilan des connaissances de la dynamique de l'érosion des côtes du Québec maritime laurentien. *Géographie Phys. Quat.* **2004**, *58*, 45. [[CrossRef](#)]
52. Bernatchez, P. Évolution Littorale Holocène et Actuelle des Complexes Deltaïques de Betsiamites et de Manicouagan-Outardes: Synthèse, Processus, Causes et Perspectives. Ph.D. Thesis, Université Laval, Ville de Québec, QC, Canada, 2003.
53. Duchesne, M.J.; Pinet, N.; Bédard, K.; St-Onge, G.; Lajeunesse, P.; Campbell, D.C.; Bolduc, A. Role of the bedrock topography in the Quaternary filling of a giant estuarine basin: The Lower St. Lawrence Estuary, Eastern Canada. *Basin Res.* **2010**, *22*, 933–951. [[CrossRef](#)]
54. Pratte, S.; Garneau, M.; De Vleeschouwer, F. Late-Holocene atmospheric dust deposition in eastern Canada (St. Lawrence North Shore). *Holocene* **2016**. [[CrossRef](#)]
55. Senneville, S.; St-Onge Drouin, S.; Dumont, D.; Bihan-Poudec, M.-C.; Belemaalem, Z.; Corriveau, M.; Bernatchez, P.; Bélanger, S.; Tolszczuk-leclerc, S.; Villeneuve, R. *Modélisation des Glaces dans L'estuaire et le Golfe du Saint-Laurent dans la Perspective des Changements Climatiques*; Technical Report; Université du Québec à Rimouski: Rimouski, QC, Canada, 2014.
56. Ruest, B.; Neumeier, U.; Dumont, D.; Bismuth, E.; Senneville, S.; Caveen, J. Recent wave climate and expected future changes in the seasonally ice-infested waters of the Gulf of St. Lawrence, Canada. *Clim. Dyn.* **2015**. [[CrossRef](#)]
57. CHS Canadian Tides and Water Levels Data Archives. Available online: <http://www.isdm-gdsi.gc.ca/isdm-gdsi/twl-mne/index-eng.htm> (accessed on 20 March 2015).
58. Saucier, F.J.; Chassé, J. Tidal circulation and buoyancy effects in the St. Lawrence Estuary. *Atmos. Ocean* **2000**, *38*, 505–556. [[CrossRef](#)]
59. Masselink, G.; Short, A.D. The effect of tide range on beach morphodynamics and morphology: A conceptual beach model. *J. Coast. Res.* **1993**, *9*, 785–800.

60. Scott, T.; Masselink, G.; Russell, P. Morphodynamic characteristics and classification of beaches in England and Wales. *Mar. Geol.* **2011**, *286*, 1–20. [[CrossRef](#)]
61. Dupuis, L.; Ouellet, Y. Pr evision des vagues dans l'estuaire du Saint-Laurent   l'aide d'un mod le bidimensionnel. *Can. J. Civ. Eng.* **1999**, *26*, 713–723. [[CrossRef](#)]
62. Didier, D.; Bernatchez, P.; Boucher-Brossard, G.; Lambert, A.; Fraser, C.; Barnett, R.; Van-Wiererts, S. Coastal flood assessment based on field debris measurements and wave runup empirical model. *J. Mar. Sci. Eng.* **2015**, *3*, 560–590. [[CrossRef](#)]
63. Stumpf, A.; Augereau, E.; Delacourt, C.; Bonnier, J. Photogrammetric discharge monitoring of small tropical mountain rivers: A case study at Riviere des Pluies, R union Island. *Water Resour. Res.* **2016**, *52*, 4550–4570. [[CrossRef](#)]
64. Harley, M.D.; Turner, I.L.; Short, A.D.; Ranasinghe, R. Assessment and integration of conventional, RTK-GPS and image-derived beach survey methods for daily to decadal coastal monitoring. *Coast. Eng.* **2011**, *58*, 194–205. [[CrossRef](#)]
65. Bracs, M.A.; Turner, I.L.; Splinter, K.D.; Short, A.D.; Lane, C.; Davidson, M.A.; Goodwin, I.D.; Pritchard, T.; Cameron, D. Evaluation of opportunistic shoreline monitoring capability utilizing existing “surfcam” infrastructure. *J. Coast. Res.* **2016**, *319*, 542–554. [[CrossRef](#)]
66. Angnuureng, D.B.; Almar, R.; Senechal, N.; Castelle, B.; Addo, K.A.; Marieu, V.; Ranasinghe, R. Shoreline resilience to individual storms and storm clusters on a meso-macrotidal barred beach. *Geomorphology* **2017**, *290*, 265–276. [[CrossRef](#)]
67. Poate, T.G.; McCall, R.T.; Masselink, G. A new parameterisation for runup on gravel beaches. *Coast. Eng.* **2016**, *117*, 176–190. [[CrossRef](#)]
68. Ojeda, E.; Guill n, J. Shoreline dynamics and beach rotation of artificial embayed beaches. *Mar. Geol.* **2008**, *253*, 51–62. [[CrossRef](#)]
69. Abessolo Ondo, G.; Almar, R.; Kestenare, E.; Bahini, A.; Houngue, G.-H.; Jouanno, J.; Du Penhoat, Y.; Castelle, B.; Melet, A.; Meyssignac, B.; et al. Potential of video cameras in assessing event and seasonal coastline behaviour: Grand Popo, Benin (Gulf of Guinea). *J. Coast. Res.* **2016**, *75*, 442–446. [[CrossRef](#)]
70. McCarroll, R.J.; Brander, R.W.; Turner, I.L.; Leeuwen, B. Van Shoreface storm morphodynamics and mega-rip evolution at an embayed beach: Bondi Beach, NSW, Australia. *Cont. Shelf Res.* **2016**, *116*, 74–88. [[CrossRef](#)]
71. Blossier, B.; Bryan, K.R.; Daly, C.J.; Winter, C. Nearshore sandbar rotation at single-barred embayed beaches. *J. Geophys. Res. Oceans* **2016**, *121*, 2286–2313. [[CrossRef](#)]
72. Wright, L.D.; Short, A.D. Morphodynamic variability of surf zones and beaches: A synthesis. *Mar. Geol.* **1984**, *56*, 93–118. [[CrossRef](#)]



  2017 by the authors. Licensee MDPI, Basel, Switzerland. This article is an open access article distributed under the terms and conditions of the Creative Commons Attribution (CC BY) license (<http://creativecommons.org/licenses/by/4.0/>).